Effects of heating rate and deposition cycle on the structural, optical, and photoelectrocatalytic properties of electrodeposited hematite films

Pannan Kyesmen[12*], William Pooe[1], Nolwazi Nombona[3], Mmantsae Diale[1*]

[1]Physics Department, University of Pretoria, Private Bag X20, Hatfield 0028, South Africa.
[2]Physics Department, Joseph Sarwuan Tarka University Makurdi (previously, Federal University of Agriculture Makurdi) P.M.B. 2373, Makurdi, Benue State, Nigeria.
[3]Chemistry Department, University of Pretoria, Private Bag X20, Hatfield 0028, South Africa.

Corresponding author's e-mail addresses: pannan.kyesmen@tuks.co.za; mmantsae.diale@up.ac.za.

Abstract.

In this research, electrodeposited hematite films were prepared at voltammetry deposition cycles of 60 and calcined at 550ºC in a furnace after ramping the temperature at the rates of 2°C/min, 10°C/min, 35°C/min, and rapid heating of about 100°C/min. Additional samples were fabricated at deposition cycles of 15, 30, and 80, and also calcined at 550ºC at a heating rate of 10°C/min. The impact of heating rate and deposition cycle number variations on the structural, optical, and photoelectrocatalytic (PEC) properties of the hematite films were assessed. All the films' X-ray diffraction (XRD) measurements showed strong peaks at the lattice planes (104) and (110), verifying hematite's rhombohedral crystal structure. The films prepared at the heating rate of 10ºC/min boosted the crystallization of the films by 47.2% relative to the ones prepared at 2ºC/min. An increase in the deposition cycle number resulted in increasing film thickness and the sample's crystallization. An indirect bandgap of 1.94-2.1 eV was estimated for the samples, with the least value obtained for the films treated at the heating rate of 10º/min and deposition cycles of 60. The same samples also yielded the largest photocurrent density of 26.2 μA/cm^2 at 1.23 V vs. reversible hydrogen electrode (RHE), while the photoanodes fabricated at 2°C/min exhibited the lowest photo-activity. The enhanced photocurrent observed for the films has been associated with high crystallinity, improved photon absorption, reduced flatband potential, and increased charge separation at the film's surface. This research underscores the importance of optimizing both the heating rate and deposition cycle numbers in the fabrication of electrodeposited photoelectrodes for PEC applications.

Keywords: Hematite nanoparticles, electrodeposition, heating rate, deposition cycle, PEC water splitting

1. Introduction.

The pursuit of sustainable and clean energy sources is necessary given the negative effects of the use of fossil fuels such as environmental pollution and global warming. Much research has been conducted in recent years towards finding clean and renewable ways of meeting the high energy needs of mankind, with solar power emerging as one of the most suitable sources due to its abundance and many means of harnessing it. PEC water splitting, one of the diverse ways of harvesting power from the sun, involves the conversion of solar energy into chemical energy in the form of hydrogen. The first decomposition of water into its components of hydrogen (H_2) and oxygen via the PEC method was presented in 1972 by Fujishima and Honda [1], where ultraviolet light was used as a light source and titanium dioxide (TiO2) as a photocatalyst. They achieved a low PEC efficiency of 0.1% partly because of the large bandgap of TiO_2 (~3.2 eV), demonstrating its inability to harvest significant photons in the visible region for photoelectrocatalysis. This motivated numerous ensuing scientists to work towards PEC hydrogen production using other photoelectrode materials such as hematite (α-Fe_2O_3), Bismuth vanadate (BiVO4) [2] tungsten trioxide (WO3) [3], and zinc oxide (ZnO) [4].

Hematite (α-Fe_2O_3), an n-type semiconducting material has been widely investigated by researchers for PEC water splitting because of its small bandgap (1.9 - 2.20 eV), high theoretical solar-to-hydrogen (STH) conversion efficiency of 17% [5], relative abundance, non-toxicity and stability in aqueous environment [6, 7]. However, limitations of using hematite as a photoanode for PEC applications such as its high electron-hole recombination rate and short hole diffusion length of about (2–4 nm) [8] result in low photoresponse during water splitting. To mitigate these challenges, nanostructuring [9] is one of the approaches that has been widely engaged in preparing hematite films with large surface areas, to facilitate charge separation and reduced electron-hole recombination during PEC applications [10, 11]. Various deposition methods have been used in preparing nanostructured hematite thin films, such as dip coating [12], spin coating [13], hydrothermal [14], spray pyrolysis [15], and electrodeposition techniques [16, 17]. The electrodeposition method is one of the easy, cheap, reproducible, and Low-temperature methods for producing films of nanostructured hematite.

The electrodeposition of hematite films using the cyclic voltammetry technique can be influenced by numerous processing parameters such as the deposition cycle numbers, annealing temperature,

annealing time, and heating rate, among others. Many studies have been reported on optimizing the synthesis of hematite nanostructures by the electrodeposition method for splitting water. Landolski *et al*. 2018, studied how the deposition cycle numbers affect the properties of hematite films, reporting an n-type behavior and bandgap values of (1.9-2.1) eV, but didn't present the PEC response of the samples [16]. For example, Zeng *et al*. 2015, produced hematite films via the electrodeposition approach and studied the effects of annealing temperature and time on the performance of hematite films, achieving an optimal photocurrent of 1.35mA/cm^2 at 1.23V vs RHE for the films calcined at 500^{o}C for 2 hours. So, the annealing temperature of electrodeposited hematite affects the crystallization process of the films [18]. However, the heating rate at which the samples are heated to get them to the annealing temperature has not been given detailed attention and is rarely reported in literature. This is regardless of the significance of the heating rate in the nucleation process of hematite films. Meanwhile, the heating rate can influence the growth mechanism, crystallization, and other microstructural properties of the films among others [19]. In light of known literature, a study that investigates the impact of heating rate on the structural and photoelectrocatalytic properties of electrodeposited hematite films is lacking. The optimization of the heating rate during the sample's annealing before the optimization of other parameters such as voltammetry cycle numbers and annealing time, can play important roles in maximizing the PEC activity of electrodeposited hematite films.

In this project, a detailed study on the influence of heating rate and voltammetry deposition cycle number on the structural, optical, and PEC properties of electrodeposited hematite thin films was investigated. Electrodeposited hematite films prepared at voltammetry deposition cycles of 60 were ramped to 550^{o}C in a furnace at a heating rate of 2°C/min, 10°C/min, 35°C/min and rapid annealing (about 100°C/min), and calcined at that temperature for 2 hrs. Additional samples were fabricated at deposition cycles of 15, 30, and 80, and annealed at 550^{o}C at a heating rate of 10^{o}C/min. These variations of the deposition cycle numbers and heating rate in the preparation of hematite films can have a notable impact on the crystallization, optical absorption, charge transport properties, and photoelectrocatalytic activity of samples. This work highlights the significance of optimizing the heating rate during annealing and the voltammetry deposition cycles, in the electrodeposition process of preparing hematite films for photoelectrocatalytic applications.

2 Experimental

2.1 Sample preparation

The electrodeposition technique was used to fabricate hematite thin films on FTO substrates. The substrates were cleaned by soaking in a soap solution for 10 min, followed by sonication in an ultrasonic bath with deionized (DI) water, methanol, and isopropanol for 15 min each. Afterward, they were rinsed with DI water and dried with nitrogen gas. The electrodeposition technique was conducted with a conventional three-electrode setup: an FTO as a working electrode, a silver/silver chloride (Ag/AgCl) in saturated 3M KCl as a reference electrode, and a 2×2 cm platinum mesh as a counter electrode. The electrodeposition solution consists of 5mM $FeCl_3$ + 5mM KF + 0.1M KCl + 1M H_2O_2 dissolved in DI water, similar to a previously reported electrolyte [20]. The electrodeposition was performed using a cyclic voltammetry technique between -0.5 and 0.5 potential vs Ag/AgCl for 60 deposition cycles to obtain Iron oxyhydrate films (FeOOH), which were then rinsed with DI water. The films were heated to 550°C in a furnace at different heating rates of 2°C/min, 10°C/min, 35°C/min, and rapid heating (about 100°C/min), and calcined for 1hr at that temperature to obtain hematite films. Following the same procedure three more samples were electrodeposited at 15, 30, and 80 deposition cycle numbers and annealed at the same temperature as previous films at heating rates of 10°C/min. the samples prepared at 15, 30, 60, and 80 deposition cycle numbers and heated at 10°C/min were denoted as ED-15C, ED-30C, ED-60C, and ED-80C respectively. **Fig. 1** gives an illustration of the fabrication process of the electrodeposited hematite samples.

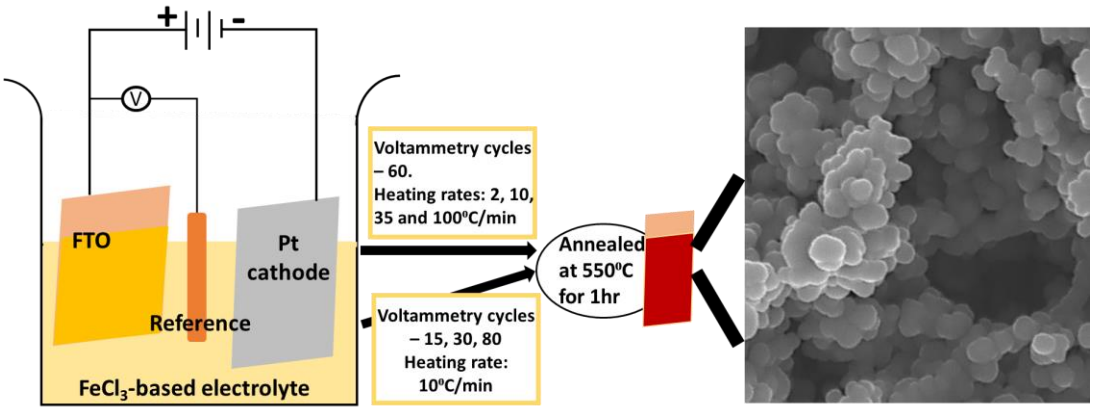

Fig. 1. An illustration of the fabrication process of the electrodeposited hematite photoanodes prepared at various heating rates and deposition cycles.

2.2 Sample characterization and PEC measurements

X-ray measurements were done to study the structural characteristics of α-Fe_2O_3 films using the Bruker D2 PHRASER diffractometer with CuKα radiation (0.15418 nm) source. Raman spectroscopy was performed using a WITec alpha 300 RAS+ confocal Raman microscope with a 523nm excitation laser at 5mW. The morphology and cross-sectional views of the α-Fe_2O_3 films were assessed using a field emission electron microscope (FE-SEM), Zeiss crossbeam 540. The cross-sectional views were examined using the ImageJ tool to deduce their approximate film thicknesses. The Zeiss equipment was connected to energy dispersive X-ray spectroscopy (EDS) was used to determine the elemental composition of the hematite films. Using a CARY 100 BIO UV-vis spectrometer, ultraviolet-visible (UV-vis) spectroscopic measurements were used to examine the optical characteristics of the films.

VersaStat 3F potentiostat was used to measure the PEC properties of the fabricated hematite nanostructures in a three-electrode cell containing sodium hydroxide (NaOH) of pH 13.6 as the electrolyte. The hematite films on FTO were used as the working electrodes, a 2x2 cm platinum meshed wire served as the counter electrode, and (Ag/AgCl) in 3M KCl was used as a reference electrode. Under dark and light conditions, linear sweep voltammetry (LSV) measurements were conducted from -0.7 V to 0.6 V vs Ag/AgCl and at 0.04 V/s scan rate to examine the photocurrent of the photoanodes. A Newport 91150V reference cell was used to calibrate the light source (a solar simulator) to 1 sun at 100 mW/cm^2 and the photoanode's illumination area of 0.49 cm^2. Under illumination at 0.23 V potential against Ag/AgCl, 10000-0.1 Hz, and with an amplitude of 10 mV, photoelectrochemical impedance spectroscopy (PEIS) measurement was performed on the photoelectrodes. To fit the impedance data from the raw analyses to a modeled circuit, ZView software for impedance spectroscopy analysis was used. Under dark conditions, Mott-Schottky analysis at a single frequency of 5000 Hz, an AC potential amplitude of 10 mV, and a DC potential interval of -1.2 to 0.6 V vs. Ag/AgCl was carried out. The commonly engaged Nernst relation was employed in converting the potential vs. Ag/AgCl scale to the RHE reference [21].

3 Results and discussion

3.1 Crystal structural and phase analysis

The structural characteristics of the prepared hematite thin films were studied using the XRD technique. The XRD measurements were conducted within 2 theta (2θ) values that ranged from

20 to 70º. The XRD patterns for the films prepared using different heating rates and at various deposition cycle numbers are shown in **Fig. 2**(a) and (b) respectively. The patterns disclosed dominant peaks at (104) and (110) planes located at 2θ values of 33.31 and 35.81º respectively, affirming the creation of hematite's rhombohedral crystal structure with lattice parameters a = b = 5.032, c = 13.733; $R\bar{3}c$ space group. Other weak peaks were also seen at (012), (113), (024), (116), (214), and (300) planes located at 2θ values of 24.28, 40.98, 49.62, 54.18, 62.54, and 64.14º respectively. The peak positions of the XRD planes agree well with the ones given in the reference standard for hematite based on the JCPDS file no. 33-0664. A comparison between the 2θ values obtained from the XRD measurements conducted on the samples and the ones given in the reference standard used in indexing the peaks is presented in Table S2. The XRD peaks for other oxides of Fe were not observed in all the XRD patterns of the samples, which indicates that the fabricated hematite films are of good quality. The intensity of the XRD peaks increases for samples prepared at heating rates of 10ºC/min and above relative to the ones fabricated at 2ºC/min. This is attributed to the significant improvement in the crystallinity of the films which narrowed the peak widths, enhancing their intensities [22]. For hematite films fabricated at various deposition cycle numbers, the intensity of the XRD peaks improved with enhancement in the number of cycles. The increase in film's crystallization with increasing deposition cycle numbers may have some effect on the XRD peak intensities due to the narrowing of the FWHM. However, in this case, the increase in the peak intensity with increasing deposition cycle numbers is largely associated with the enhancement in the film's thickness with the number of deposition cycles, similar to previous reports [16, 23].

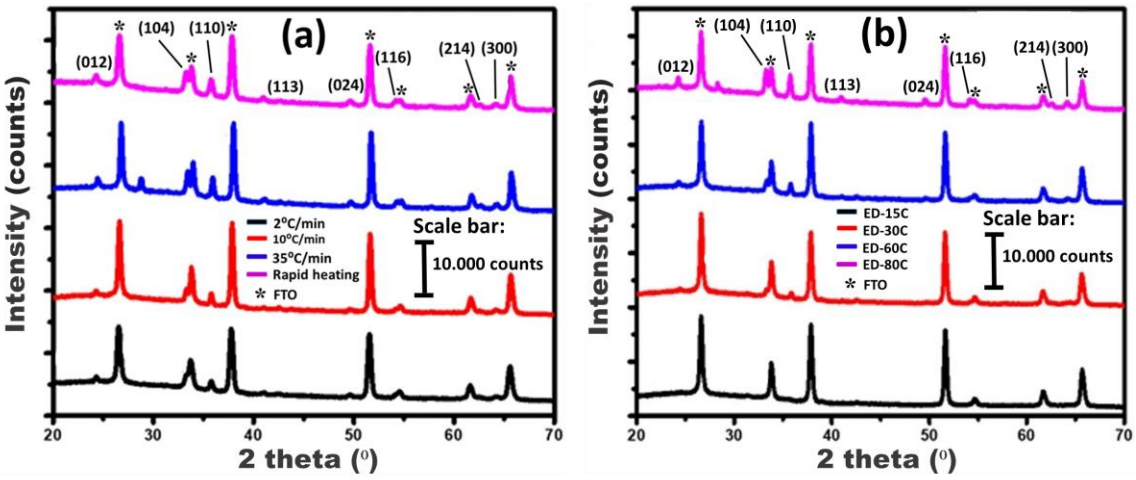

Fig. 2. XRD pattern of electrodeposited hematite films fabricated at various (a) heating rates and (b) deposition cycles.

The XRD peaks at (110) planes were examined to extract the estimated full width at half maximum (FWHM) and the crystal size (*D*) values of the hematite samples. The estimated crystal size (*D* values deduced for the samples were evaluated using the Debye-Scherrer relation presented in Equation 1:

$$D = \frac{k\lambda}{\beta cos\theta} \quad (1)$$

where *k* denotes the Scherrer constant given as 0.9, the wavelength is represented by λ with incident X-ray of Cu-Kα radiation of 0.15418 nm, β represents the FWHM, and θ is the Bragg angle or peak position. Also, the microstrain, ε, and dislocation density, q, of the hematite samples were examined using Williamson and Smallman's approach to extract additional insight into the structural characteristics of the films [24]. The results obtained for D, ε, and ɋ parameters for the electrodeposited hematite films are given in **Fig. 3**(a), (b), and (c) respectively, as well as in **Table S1.**

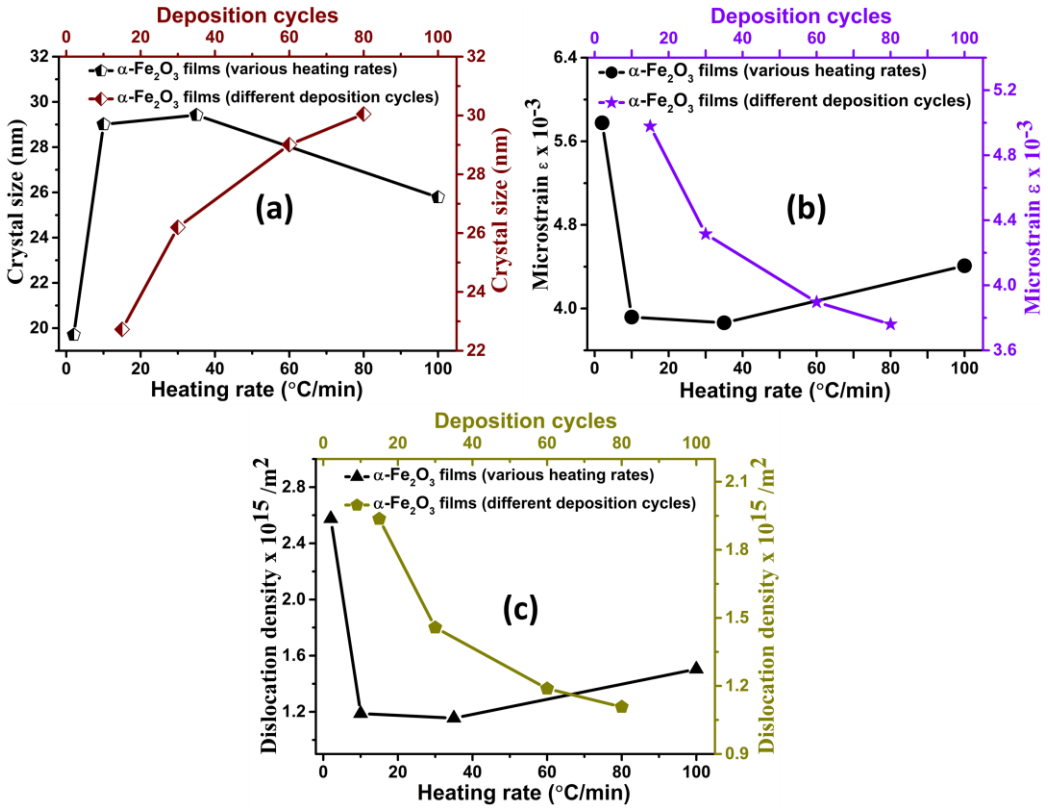

Fig. 3. The (a) crystal size, (b) microstrain, and (c) dislocation density of the hematite films prepared at various heating rates and deposition cycles.

The heating rate shows a notable impact on the structural characteristics of the electrodeposited hematite films. Annealing of the films at the rate of 2ºC/min yielded the least crystal size of 19.7 nm. This is attributed to the slow nucleation process that affected initial crystal growth at this heating rate [19]. An increase in the heating rate to 10ºC/min boosted the crystal size of the films by 47.2%. An increase in the heating rate to 35ºC/min did not yield any noticeable improvement in the crystallite size of the films. Further increase of the heating rate to 100ºC/min (rapid heating) led to an 11.0% drop in the film's crystallite size relative to the value obtained for the sample that was treated at 10ºC/min. This indicates that the heating rate of 100ºC/min is above the critical value required for the optimal crystallization of the hematite films, causing a decline in the growth rate of the film's crystallites [25].

The proposed mechanism through which heating rate influences the nucleation process and consequently the crystal size of the particles is explained based on the correlation that relates the nucleation temperature as a function of the heating rate. For the crystallization of SiO_2 and other materials processing that involves phase transformations via heat, it has been shown that the nucleation temperature increases with increasing heating rate up to a certain critical point, in which the system can maintain thermal stability [25]. So, at much lower heating rates the nucleation temperature is low, and atomic diffusion becomes limited, thereby hampering the film's overall crystallization. Below the particle's critical nucleus radius, an increase in heating rate will cause an increase in the particle size. At heating rates where the particle nucleus is of a supercritical size, energy is released if further nucleation attempts to occur, in line with the classical nucleation theory [26], thereby causing no further particle growth. Heating rates larger than the critical value make the critical nucleus radius increase rate become more than the growth rate of the nuclei, causing no further nucleation to occur. This is because, if the critical nucleus radius of the particle is of subcritical size, it costs energy to increase the particle's size whereas, if the particle's nucleus is supercritical, energy is released when the particle attempts to grow further [27]. So, for the hematite films processed at a low heating rate of 2 ºC/min, the nucleation temperature is low and the atomic diffusion becomes limited, thereby hampering the film's overall crystallization. It also indicates that the heating rate is below the critical value. Meanwhile, the samples prepared at

heating rates of 100 ºC appear to be beyond the critical value leading to a decline in the film's crystallization.

Similarly, the microstrain and the dislocation densities yielded the highest values for hematite films treated at 2ºC/min. After increasing the heating rate to 10ºC/min, a drastic decrease in the ε and d values of 32.2 and 53.9% was observed for the samples respectively. This is linked with the reduction of grain boundaries and the amount of defects in the films due to improved crystallization [16, 28]. An increase in the heating rate to 35ºC/min did not yield any significant further decrease in the ε and d values of the electrodeposited hematite films. Rapid heating at about 100ºC/min produced a 12.5 and 26.1% increase in the ε and d relative to the values evaluated for the samples treated at 10ºC/min, respectively. This is an indication of an increase in the number of imperfections present in the film's lattice [28].

The deposition cycle shows a consistent impact on the D, ε, and d values estimated for the electrodeposited hematite films. The crystal size values increase with increasing deposition cycle numbers. This is caused by the enhancement of the film's thickness with increasing deposition cycle numbers, which is displayed in the cross-sectional images of the films in section 3.2 (Fig. 6). It has been established theoretically by the statistical model of crystallization given by the modified Kolmogorov–Johnson–Mehl–Avrami (KJMA) that thinner films can slow the crystallization process. This has also been affirmed experimentally for hematite [16] and other materials [29-31]. An increase in the number of deposition cycles will consequently cause an enhancement in the amount of nucleation sites that induces the surface diffusion and migration of more ad-atoms which causes increased coalescence, improving grain growth [32, 33]. Improved crystallization can enhance the electron mobility and charge separation efficiency of the films in PEC applications [28]. Meanwhile, the evaluated ε and d values decrease with the increasing deposition cycle numbers. This is caused by the improvement of the film's crystallization with enhanced deposition cycle numbers. Generally, a reduced ε is an indication of lowered stress in the film's lattice, while a decreased d value implies a drop in the amount of lattice imperfection in the films. These lattice disorder that results from the poor crystallization of the films can create a negative effect when the material is applied in PEC reactions because they can serve as locations for charge carriers' recombination [34, 35].

3.2 Surface morphology and elemental distribution analysis

The SEM micrographs of the electrodeposited hematite films treated at different heating rates are shown in **Fig. 4**(a) - (d). The micrographs disclosed agglomerated spherical nanoparticles at the surface of the films. The films prepared at 2 and 10ºC/min heating rates appear to have slightly porous surfaces, based on the visual inspection of the film's micrographs. However, heating rates of 35ºC/min and above caused the development of more compact nanoparticles that are also agglomerated at the surface of the films. The mean grain sizes of the films were not estimated because of the high aggregation of the nanoparticles, which can distort their accurate evaluation. High particle agglomeration can serve as locations for charge carriers to recombine, reducing the efficiency of photoelectrodes during PEC water splitting. This is because the huge size increase of the aggregated particles reduces their surface-to-volume ratio, which favours surface recombination. More so, the aggregation of the nanoparticles can limit the volume fraction of the aggregates that get irradiated due to the low penetration depth inside the aggregates, which can further inhibit the generation of charge carriers and photocatalytic activity [36]. The SEM images showing the surface morphology of the electrodeposited hematite films produced at various deposition cycles and a constant heating rate of 10 ºC/min are given in **Fig. S1**(a) - (d). Also, based on the visual inspection of the film's images, the surface morphology of the films was not significantly influenced by the number of deposition cycles as they all revealed highly agglomerated nanoparticles that are slightly porous. It is expected that an increase in the particle sizes of the films with increasing deposition cycle numbers or heating rate (Fig. 3a and Table S1) will result in the formation of more compact and uniform film surfaces. This didn't happen probably because of the high aggregation of the nanoparticles on the film surface, which doesn't seem to be impacted by the particle size of the films. Further investigations may yield a better understanding of the reason for the behavior.

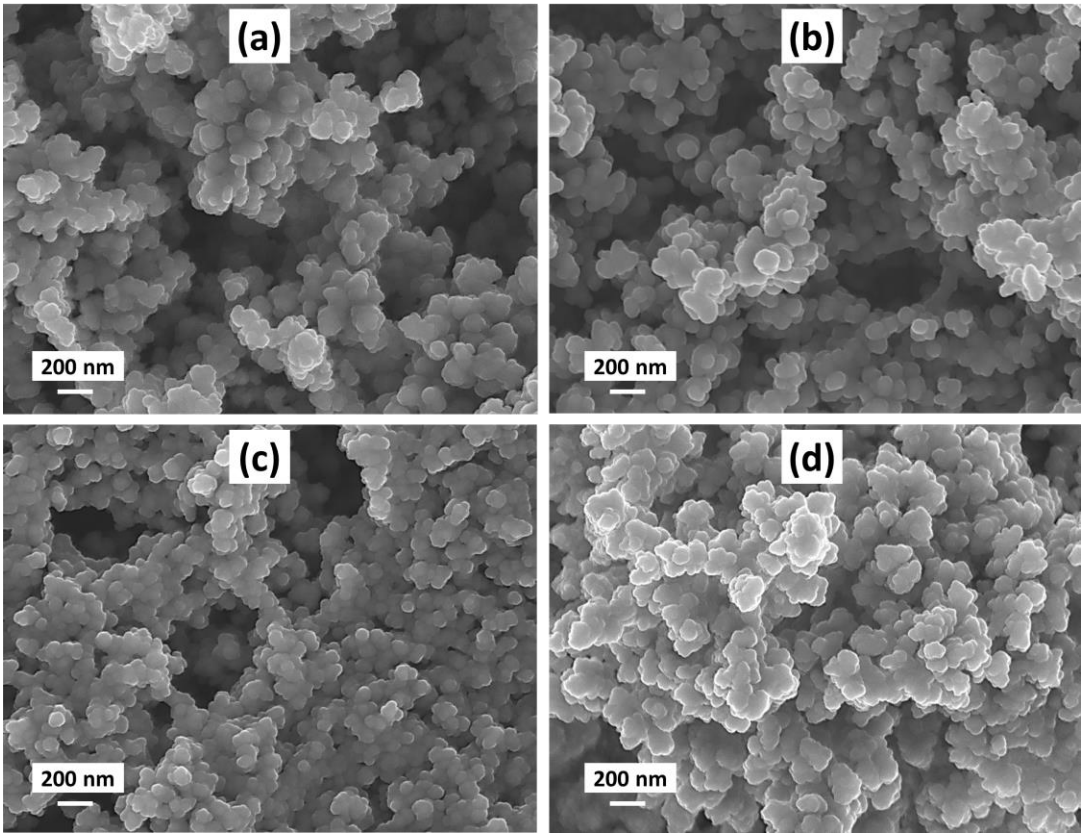

Fig. 4. SEM micrographs of hematite films produced at various heating rates of (a) 2ºC/min, (b) 10ºC/min, (c) 35ºC/min, and (d) rapid heating (about 100°C/min).

The elemental compositions of the hematite thin films were verified by means of EDS studies. The results for samples prepared at different deposition cycles are given in **Fig. S2**(a) - (d) in the supplementary document. The EDS analysis was used to examine the presence of any potential contaminants in the films. The results show that all of the samples had both iron (Fe) and oxygen (O), which are the constituent elements of the nanostructured α-Fe_2O_3 films. Tin (Sn) was also detected since FTO substrates contain Sn as one of its elements. Other impurity elements were not observed in the EDS analysis, asserting the good purity of the hematite films prepared. So, all the samples consist of the same constituent materials regardless of deposition cycles. This further affirms the nucleation and growth of hematite films, besides the XRD results.

The morphology of the cross-section of the electrodeposited samples prepared at various deposition cycle numbers is presented in **Fig. 5**(a) - (d). The films become thicker with an increasing number of deposition cycles as anticipated, similar to previous observations [16, 37].

The ED-15C samples yielded the least film thickness of 248 ± 36 nm which increased by about 165% for the ED-80C films. The optimization of the thickness of hematite films is paramount for its application in photoelectrocatalysis. This is because of the paradox between the low absorption coefficient of hematite, requiring thicker films (~ 400 nm) for sufficient light absorption, and its short diffusion length of 2-4 nm, which promotes charge recombination [38, 39]. In addition, the thickness of the films also affects their crystallization. An increase in the film's thickness enhances the crystallite size of the films as shown in Fig 5(e). The samples prepared at different heating rates were all deposited using 60-voltammetry cycles and treated at the same temperature and duration. So, in view of this, the cross-section of the films was not examined since the thickness of the films was not expected to have any significant difference.

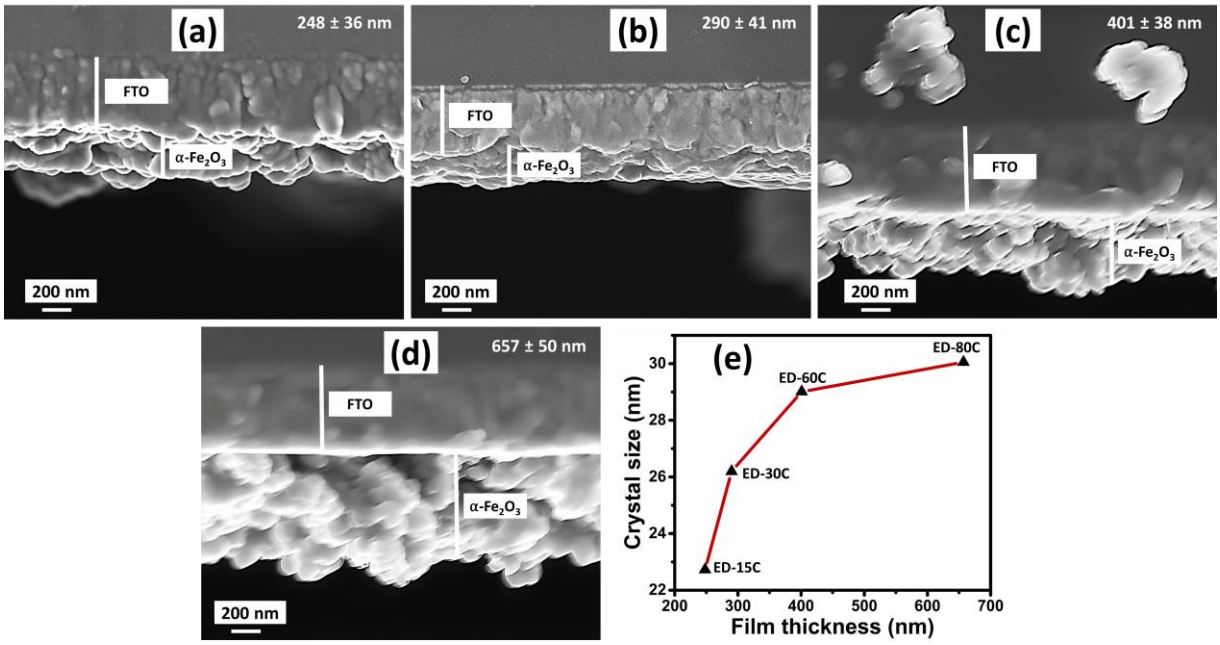

Fig. 5. Cross-sectional images obtained from SEM for hematite films fabricated at (a) 15C, (b) 30C, (c) 60C, and (d) 80C deposition cycle numbers respectively, while (e) presents a plot of the crystal sizes of the films against their various approximate thicknesses.

3.3 Optical absorption and bandgap evaluation

Studies with UV-Vis spectroscopy were conducted on the electrodeposited hematite samples to obtain their optical absorption and deduce their indirect bandgap values. The plots of normalized absorbance against wavelength are given in **Fig. 6**(a) and (b) for the films synthesized at different heating rates and deposition cycle numbers respectively. The pattern of the film's absorption

disclosed $^6A_1$ – $^4E_1$, $^4A_1$ ligand field transitions with peaks at about 406 nm wavelengths, which has been associated with a single Fe^{3+} cation. Another transition that has been linked to the double exciton processes that are related to Fe^{3+} – Fe^{3+} cation pairs resulted in the defined peaks at 546 nm observed for the films [40]. For films treated at different heating rates, enhanced photon absorption was particularly observed for the samples treated at 10º/min. This is linked to the improved crystallization of the films coupled with better light scattering due to the porous surface observed for the films. Light absorption was observed to improve with increasing number of deposition cycles which is related to the increment in the thickness of the films. The ED-80C samples show absorbance saturation because of the huge thickness of the films [41]. Photon absorbance can get saturated when the travel path length becomes too long, causing non-linearity and deformation of the absorption pattern [42].

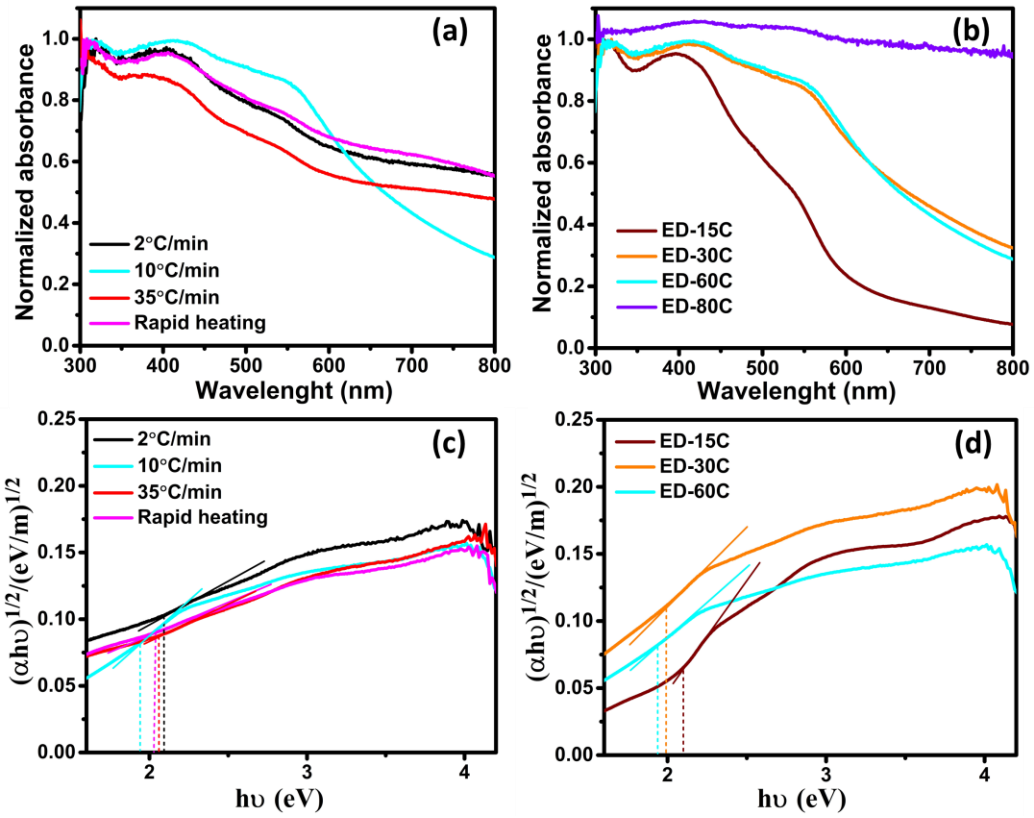

Fig. 6. The UV-Vis normalized absorbance of hematite films processed at (a) different heating rates and (d) deposition cycle numbers: (c) and (d) present the plots from the Tauc estimation of the indirect bandgap of the films, respectively.

The indirect bandgaps were estimated using the widely engaged Tauc approximation [43-45] and the plots are displayed in **Fig. 6**(c) and (d) for the samples fabricated at various heating rates and deposition cycle numbers respectively. The least approximate bandgap of 1.94 eV was estimated for the samples treated at 10º/min heating rate while the highest value of 2.10 eV was estimated for the ones prepared at 2º/min. This is mainly attributed to the drop in the crystallite size observed for the 2º/min treated films, which decreases the attenuation coefficient of light (at shorter wavelengths, λ < 600 nm), resulting in limited photon absorption and increased bandgap [28, 46]. Regarding the samples produced at varying deposition cycles, the bandgap values reduce with increasing cycle numbers. This is consistent with other observations in literature [23, 47, 48]. The cause for this behavior can be linked to the inbuilt electric field around the defects in the films or the quantum confinement effects that result from improved crystallization of the films with increasing deposition cycles and film thickness [49]. However, since the films yielded similar surface texture and experienced a decrease in their dislocation densities and lattice imperfections with increasing deposition cycle numbers, the cause of this behavior is largely ascribed to the quantum confinement effects [50, 51].

3.4 Photoelectrochemical characteristics

Mott-Schottky (M-S) studies were done to assess the impact of heating rate and deposition cycle numbers on the flatband potential, V_{fb}, and donor density N_D, of the electrodeposited hematite samples. M-S plots for the samples fabricated at different heating rates and deposition cycle numbers are displayed in **Fig. 7**(a) and (b) respectively. The M-S relation given in Equation S1 of the supplementary data in conjunction with the data extracted from the plots was used to deduce the values for V_{fb} and N_D of the hematite photoanodes. Details of the evaluation process followed in deducing the V_{fb} and N_D values are present in the supplementary information. **Table 1** presents the approximate values for V_{fb} and N_D calculated for the hematite films.

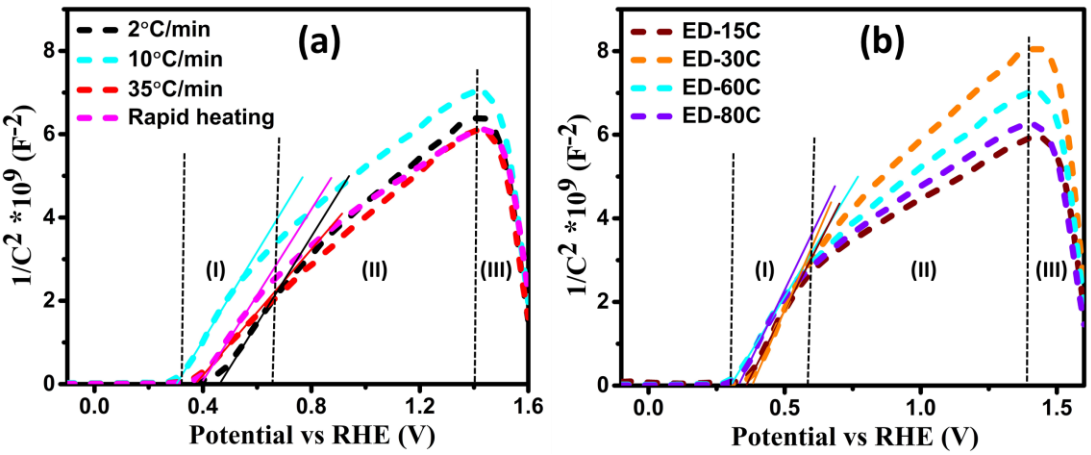

Fig. 7. M-S plots of hematite photoanodes fabricated at various (a) heating rates and (b) deposition cycles.

Table 1. The flatband potential and donor density of electrodeposited hematite photoanodes fabricated at different heating rates and deposition cycles.

Sample	**V_{fb} vs RHE (V) in 1 M NaOH**	**$N_D * 10^{19}$ (cm^{-3})**
2°C/min	0.424	5.6
10°C/min	0.279	5.0
35°C/min	0.334	7.8
Rapid annealing	0.359	5.5
ED-15C	0.332	4.1
ED-30C	0.348	3.8
ED-60C (10°C/min)	0.279	5.0
ED-80C	0.292	4.6

The variation of heating rates during the sample's preparation shows a notable impact on the V_{fb} of the electrodeposited hematite samples. The samples treated at 2°/min produced the most positive V_{fb} value, caused by the poor crystallization observed for the films [28]. An increase in the heating rate to 10°/min yielded the most negative V_{fb} of 0.279 V vs. RHE, representing a 34.2% decrease relative to the value obtained for the samples treated at 2°/min. A more negative V_{fb} value can help reduce the external bias required to initiate PEC reactions and improve charge carrier separation, promoting the photoactivity of photoanodes [52, 53]. A further increase in the heating rate to

35º/min and 100º/min yielded a 21.2 and 15.3% drop in the V_{fb} values obtained for the films respectively, when compared to the value estimated for the films treated at 2º/min heating rate. A much smaller drop was observed for the films treated at 100º/min because of the drop in the film's crystallization due to the slowing down of the film's nucleation rate resulting from rapid heating [27]. The preparation of the hematite photoanodes at varying deposition cycles showed some impact on the flat band potential of the films. The ED-60C and ED-80C samples yielded a 15.9 and 12.0% decrease in their V_{fb} values relative to the approximate value obtained for ED-15C photoanodes, respectively. This is also associated with the enhancement in the crystallite size of the films. An improvement in the crystal size of the films will result in a decrease in the density of grain boundaries which will reduce the resistance of the films, leading to a decrease in the flatband potential [28, 52]. The changes in the heating rate and deposition cycle numbers during the preparation of the hematite films impacted their crystal sizes, which explains the variations in the V_{fb} values evaluated for the films.

The donor density of the electrodeposited hematite films was not significantly altered by the variation of heating rates during the sample's preparation, yielding N_D values in the order of 10^{-19} cm^{-3}. The variation of the deposition cycle numbers in the fabrication process of the electrodeposited hematite films showed a slight impact on the estimated N_D values of the films. The ED-60C and ED-80C samples increased by a factor of 1.24 and 1.12 relative to the approximate value obtained for ED-15C photoanodes, respectively. This is also attributed to the boost in crystallinity observed for the films which limited the number of unwanted lattice defects in the films. These defects are higher in much thinner films (ED-15C) due to poor crystallization and act as locations for trapping and immobilization of charge carriers, which reduces their lifetime and limits the number of carriers that will be available for conduction [51]. The approximate N_D values obtained for all the films ranged from 3.8 to 57.8 × 10^{-19} cm^{-3}, similar to other reported values for the pristine hematite.

Generally, the M-S plots disclosed three distinct linear regions which have been marked as I, II, and III as shown in **Fig. 7**. As expected, the positive slopes observed for all the samples in regions I and II are indicative of the n-type property of the fabricated hematite films. The slope in regions I and II represent the shallow and deep donor levels respectively, similar to many other reports for hematite films [54-56]. The shallow donor level is located between the conduction band minimum

(CBM) and the Femi level and consists of states that ionize at the flatband potential. The deep donor level lies below the Fermi energy, within the bandgap, and the states are not ionized at the flatband potential [55, 56]. A more detailed description of the linear regions I and II has been given in a previous report for hematite [56]. In the third region of the M-S plots, the hematite films exhibit a negative slope indicating a switch to a p-type semiconducting behaviour, at a higher positive potential of about 1.45 V vs RHE. This is attributed to the reduction of F^{3+} to F^{2+} at higher potentials, resulting in the formation of FeO which is a p-type material [57, 58].

Measurements using LSV were taken in the dark and light of 1 sun to deduce the photocurrent density of the hematite photoanodes. The results are presented for the photoanodes prepared at various heating rates and different deposition cycle numbers in **Fig. 8**(a) and (b) respectively. The photoanodes processed at 2ºC/min produced the lowest photocurrent of 7.9 μA/cm^{-2} at 1.23 V vs. RHE. This is caused by the poor crystallization of the films which increases grain boundaries and reduces their conductivity [28]. The films also show current saturation across all the scanned potential values. This is an indication of high charge carrier's recombination which is caused by the high grain boundaries coupled with the huge particle agglomeration on the film's surface [59, 60]. The samples prepared at 10ºC/min heating rate and 60 deposition cycles produced the largest photocurrent of 26.2 μA/cm^2 at 1.23 V vs. RHE. The combined effects of improved crystallization, reduced flat band potential, and increased photon absorption lead to the boosted photocurrent response for the samples. Further attempts to optimize the thickness of the films through the variation of the deposition cycles during sample preparation still yielded the best photoresponse for the ED-60C photoanodes treated at 10ºC/min. The thickness of the films impacts the PEC activity of hematite photoanodes because of the paradox between their poor absorption coefficient and short diffusion length. The poor absorption coefficient of hematite requires films with a minimum thickness of 400 nm to ensure sufficient light utilization for PEC reactions [38]. On the other hand, the short diffusion length of hematite (2-4 nm) [61] means thicker films will lead to the recombination of most photogenerated charge carriers within the bulk of the films. This paradox coupled with the role of film thickness on the sample's crystallization and PEC response motivates the optimization of the film's thickness through the variation of deposition circle numbers.

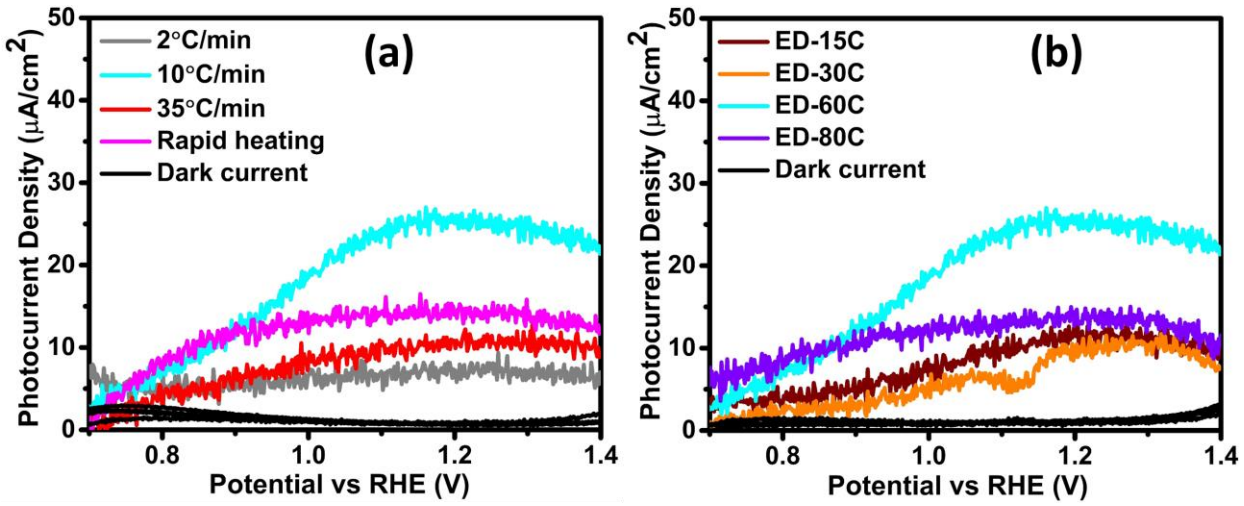

Fig. 8. Photocurrent density of the hematite samples processed at varying (a) heating rates and (b) deposition cycles.

In general, the high particle agglomeration observed across all the prepared electrodeposited films coupled with the low annealing temperature is largely responsible for the generally poor photoactivity observed for the samples. The photocurrent of the samples can be further boosted by exploring ways of limiting the particle agglomeration on the film's surface. Also, annealing of the films at a high temperature of 700ºC or above can further induce improved crystallinity and conductivity of the films, which will also further boost the photocurrent response [62]. However, this can result in the unintentional doping of the hematite films thereby influencing the characteristics and PEC response of the films. The annealing temperature of 550ºC was selected to avoid the unintentional doping of the samples to enable for a targeted study of the influence of the heating rate and deposition cycles on the properties of pristine hematite films.

PEIS was conducted to extract some data on the charge transport behavior on the surface and bulk of the electrodeposited hematite samples. **Fig. 9**(a) and (b) give the PEIS Nyquist graphs for the samples synthesized at various heating rates and deposition cycles respectively. The ZView software was adopted to fit the raw PEIS data set to a modeled circuit shown in the insets of **Fig. 9.** The circuit element symbolized by Rs is the series resistance due to the FTO contact, external wires, and the ions in the electrolyte [63]. Rbk and Rct denote the resistance to charge transport within the film's bulk and charge transfer at their surfaces respectively. The constant phase elements CPE-b and CPE-s stand for the space charge region's capacitance and surface states

respectively [64, 65]. The CPE-T components of the CPE elements are generally described as the Q-value, while the CPE-P is the pseudo-capacitance factor that can only have values from 0 to 1 [66]. The actual capacitance (C) values of CPE-b and CPE-s components were calculated using the relation $C = Q^{1/s} \times R^{(1-s)/s}$ [67] and presented as Cb and Css respectively, where R is connected parallel resistance to the CPE components and s is their CPE-P value. The calculated values acquired for each of the circuit elements and the defined Cb and Css for the various samples are presented in **Table 2**.

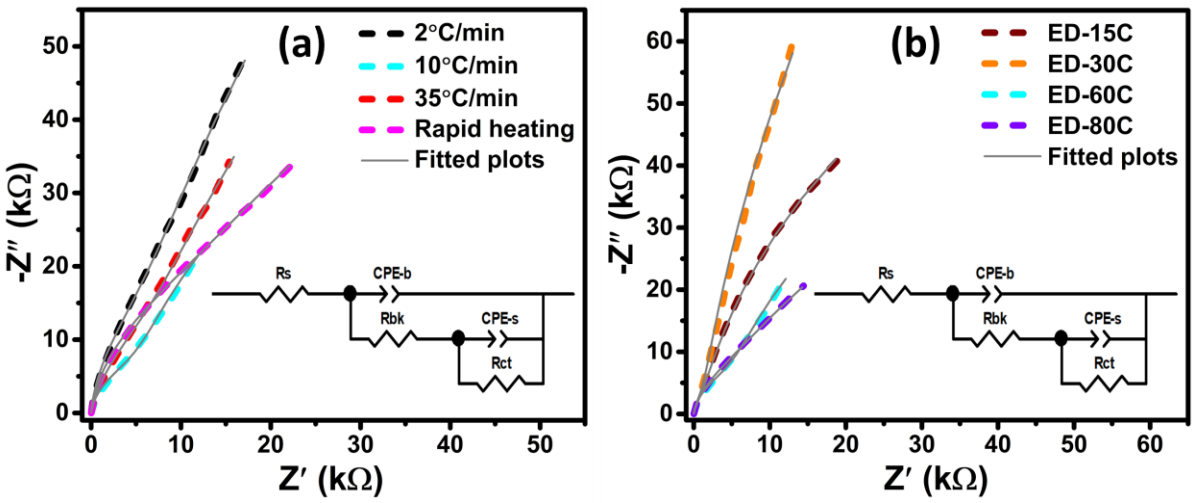

Fig. 9. PEIS plots of electrodeposited hematite samples produced at various (a) heating rates and (b) deposition cycles. The inset of the plots gives the circuit model used in fitting the raw data set.

Table 2. The estimated values deduced for the separate elements of the modeled equivalent circuit used in fitting the raw PEIS data set of the electrodeposited hematite films.

Sample	Rs (Ω)	CPE-a		Ca (mF)	Rbk (kΩ)	CPE-b		Cb (mF)	Rct (kΩ)
		T (mF)	P			T (mF)	P		
2°C/min	9.80	0.020	0.96	0.020	47.97	0.015	0.92	0.017	296.00
10°C/min	9.55	0.027	0.94	0.025	14.51	0.045	0.91	0.051	99.48
35°C/min	8.02	0.025	0.90	0.025	37.11	0.021	0.91	0.024	220.00
Rapid annealing	9.94	0.022	0.94	0.021	41.01	0.033	0.85	0.042	130.00
ED-15C	7.50	0.021	0.93	0.018	9.11	0.012	0.84	0.014	176.00

ED-30C	10.77	0.016	0.97	0.015	9.02	0.010	0.88	0.013	628.00
ED-60C (10ºC/min)	9.55	0.027	0.94	0.025	14.51	0.045	0.91	0.051	99.48
ED-80C	7.98	0.032	0.90	0.031	20.83	0.045	0.80	0.062	85.50

For hematite films prepared at various heating rates, the Rct yielded the least value for the photoanodes treated at 10ºC/min while its surface state capacitance, Css was the highest. This justifies the relatively high photoresponse attained by the photoanodes as low Rct and high Css are favourable properties that facilitate charge carriers separation at the film's surface during photoelectrocatalysis. This further explains the high photocurrent density recorded for the electrodeposited samples fabricated at 10ºC/min heating rate. The photoanodes synthesized at 2ºC/min heating rate produced the largest Rct and least Css values among films prepared at various heat ramping rates. This further explains the low photoresponse observed for the samples. For the films prepared at various deposition cycles, the ED-80C samples exhibited slightly lower Rct and higher Css values relative to the value obtained for the ED-60C (10ºC/min) samples. However, the ED-80C films show a 43.6% increase in the bulk resistance, Rbk, when compared to the value recorded of ED-60C samples. This is because of the huge thickness of the ED-80C films, which causes high rate of recombination of generated charge carriers in the bulk of the samples and limits their movement to the film's surface. This gives the reason for the low photocurrent observed for the ED-80C films relative to the ED-60C samples despite yielding lower Rct and Css values. This can be more explicitly seen in the expanded view of the PEIS plots for the samples fabricated at various heating rates shown in **Fig. S3**.

The energy band response, the mechanisms linked to the transport of charge carriers, and the photo-induced reactions that occur in the bulk and on the surface of the hematite photoanodes and at the counter electrode during photoelectrocatalysis, are presented in **Fig. 10**. The photoanode undergoes various processes associated to charge transfer before reaching equilibrium when submerged in a liquid electrolyte. While the electrons surrounding the material's surface are driven toward the solution, the electrolyte's ions are absorbed at the interface of the hematite photoanodes. This will lead to the formation of an electric field-characterized depletion area near the film's surface [68, 69]. Furthermore, the valence band (VB) and conduction band (CB) will bend upward

because of the electric field within the depletion area. The implication of the band bending is such that holes are more easily able to go from the VB to the film's surface while limiting the electron's movement from the CB to the rear FTO contact [70]. Additionally, the Helmholtz layer, a much tiny area of absorbed ions gets formed next to the electrode's surface [68]. Photo-induced electron-hole pairs are produced in the hematite films during photoelectrocatalysis when the photon's energy is equal to or above its bandgap. The holes are then driven from the VB of the hematite photoanode to its surface, where they perform a water oxidation reaction (OER) to release H^+ in the electrolyte. The electrons are driven to the FTO contact from the CB of hematite and further to the Pt counter electrode through an external wire connection, where they reduce H^+ to produce H_2. The depletion layer's inherent electric field speeds up the transport of holes to the hematite's surface, the separation of charge carriers, and the transport of electrons to the FTO contacts.

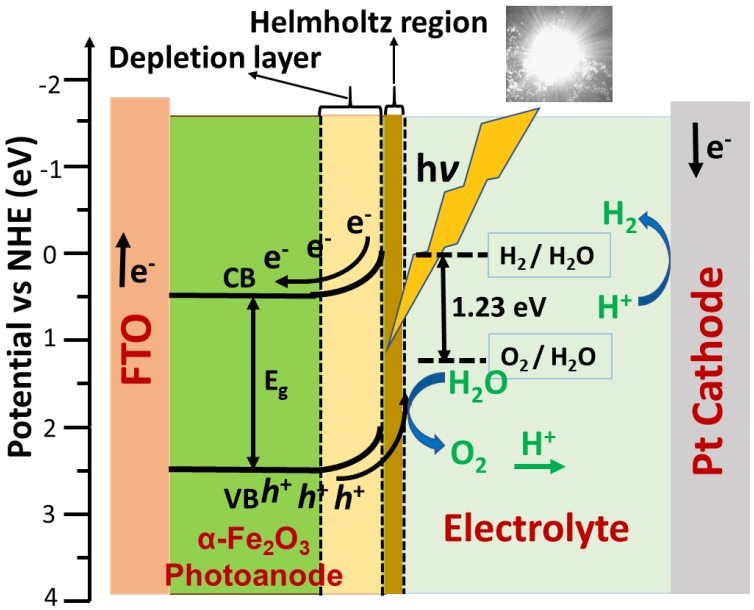

Fig. 10. Energy band bending, charge transport, and reaction mechanisms of the fabricated hematite photoanodes.

The characteristics of the hematite films can play key roles in determining the rate of OER on the hematite's surface, which is central to the material's PEC performance. The modification of the heating rate and deposition cycle numbers has enhanced the crystallinity, reduced grain boundaries, and limited dislocation density and microstrain for the films treated at 10ºC/min. These improved properties contributed in different ways to the improved OER reaction and PEC response

observed for the films. The improved crystal size observed for the films enhanced the material's conductivity. It is also responsible for the reduced flatband potential and boosted charge separation efficiency observed for the films [28, 51]. The limited dislocation density and microstrain observed for the films indicate a reduction of undesirable defects in the films that could act as charge trapping and recombination centers during PEC reactions [34, 35]. The improved surface texture that yielded reduced grain boundaries also contributed to inhibiting high surface recombination of charge carriers [59]. Meanwhile, the reduced bandgap and enhanced light absorption exhibited by the films boosted the number of photogenerated charge carriers that will be available to participate in PEC reactions [71]. These improved properties combine to yield the enhanced OER rate and PEC response observed for the photoanodes fabricated at 10 ºC/min and deposition cycle of 60. This is evident in the enhanced photocurrent (**Fig. 8**) and reduced charge transfer resistance (**Table 2**) observed for the samples.

Generally, the optimum photocurrent response of 26.2 μA/cm^2 at 1.23 V vs. RHE observed for the hematite films prepared in this work is low because of the high particle agglomeration on the film's surface and low processing temperature. However, this compares well with some reported values in the literature, for hematite films prepared at similar annealing temperatures with the one used in this project [43, 53, 62, 72]. A photocurrent density of less than 5 μA/cm^2 at 300 V vs. saturated calomel electrode (SCE) was reported by Vanags *et al*. 2015, for electrodeposited films of compact hematite nanoparticles, which was annealed at 450ºC for 1 hr [53]. Nyarige *et al.* 2020, reported a low photocurrent density of 6.4 μA/cm^2 at 1.23 V vs. RHE, for pristine hematite films of compact nanograins synthesized via spray pyrolysis and annealed at 450ºC for 1 hr [43]. Wu *et al.* 2022, also reported a low photocurrent of 6 μA/cm^2 at 1.23 V vs. RHE for hematite nanorods fabricated using a simple sonochemical approach and annealed at 550ºC for 2 hr [62]. Generally, the PEC response of pristine hematite photoanodes is low due to the poor conductivity, charge transfer kinetics, and other intrinsic properties of hematite. It is often difficult to modify the intrinsic properties of hematite without engaging the concepts of doping [17], heterojunction formation [73], the use of co-catalyst [74], and elevated temperature annealing [62], among other strategies. This research work attained a noticeable improvement in the photoactivity of pristine hematite films through the optimization of the heating rate and deposition cycle numbers for electrodeposited films. The research presents for the first time, the critical roles that heating rate plays in the preparation of electrodeposited hematite and its nucleation process. It showcases the

need to closely investigate the heating rate in many solution-based syntheses of pristine nanostructured materials for photo-based applications, prior to any further modifications through doping and heterojunction formation among others. This project also underscores the significance of optimizing the film's thickness for PEC applications.

4 Conclusions

In this project, the impact of heating rate and deposition cycle number on the structural, optical, and PEC properties of the hematite films were studied. Hematite photoanodes were prepared using electrodeposition at voltammetry deposition cycles of 60 and annealed at 550^{o}C in a furnace for 1hr after the rates 2°C/min, 10°C/min, 35°C/min, and rapid heating (100°C/min). More samples were prepared at deposition cycles of 15, 30, and 80, and annealed in a similar manner as the previous samples but at a constant heating rate (10^{o}C/min). The rhombohedral structure of hematite was affirmed by XRD results which disclosed peaks at lattice planes (104) and (110). The films prepared at the heating rate of 10^{o}C/min boosted the crystallization of the films by 47.2% relative to the ones prepared at 2^{o}C/min. The crystal size values increase with increasing deposition cycles caused by the increment in the thickness of the samples. FE-SEM results revealed spherical hematite nanoparticles which are highly agglomerated. The bandgap estimated for the films ranges from 1.94-2.1 eV, with the lowest value obtained for the films treated at the heating rate of 10^{o}/min and deposition cycles of 60. The same samples also yielded the optimum photocurrent density while ones fabricated at 2°C/min gave the lowest photoresponse. The enhanced photocurrent observed for the films has been associated with high crystallinity, improved photon absorption, reduced flatband potential, and boosted separation of charges at the surface of the films. This study highlights the significance of optimizing the heating rate and deposition cycle numbers during the fabrication of photoelectrodes for PEC applications via the electrodeposition method.

Acknowledgments

The authors acknowledge support from the University of Pretoria (UP) and financial assistance from the externally funded postdoctoral program at UP: grant cost center: A1E689, and the South African Research Chairs Initiative (SARCHI), UID; 115463.

Reference

[1] A. Fujishima, K. Honda, Electrochemical photolysis of water at a semiconductor electrode, Nature, 238 (1972) 37-38. https://doi.org/10.1038/238037a0.

[2] J. Ravensbergen, F.F. Abdi, J.H. Van Santen, R.N. Frese, B. Dam, R. Van De Krol, J.T. Kennis, Unraveling the carrier dynamics of BiVO4: a femtosecond to microsecond transient absorption study, J. Phys. Chem. C, 118 (2014) 27793-27800. https://doi.org/10.1021/jp509930s.

[3] F.M. Pesci, A.J. Cowan, B.D. Alexander, J.R. Durrant, D.R. Klug, Charge carrier dynamics on mesoporous WO3 during water splitting, J. Phys. Chem. Lett., 2 (2011) 1900-1903. https://doi.org/10.1021/jz200839n.

[4] M. Liu, C.-Y. Nam, C.T. Black, J. Kamcev, L. Zhang, Enhancing water splitting activity and chemical stability of zinc oxide nanowire photoanodes with ultrathin titania shells, J. Phys. Chem. C, 117 (2013) 13396-13402. https://doi.org/10.1021/jp404032p.

[5] P. Dias, A. Vilanova, T. Lopes, L. Andrade, A. Mendes, Extremely stable bare hematite photoanode for solar water splitting, Nano Energy, 23 (2016) 70-79. https://doi.org/10.1016/j.nanoen.2016.03.008.

[6] B. Klahr, S. Gimenez, F. Fabregat-Santiago, T. Hamann, J. Bisquert, Water oxidation at hematite photoelectrodes: the role of surface states, J. Am. Chem. Soc., 134 (2012) 4294-4302. https://doi.org/10.1021/ja210755h.

[7] A.A. Yadav, T. Deshmukh, R. Deshmukh, D. Patil, U. Chavan, Electrochemical supercapacitive performance of Hematite α-Fe2O3 thin films prepared by spray pyrolysis from non-aqueous medium, Thin Solid Films, 616 (2016) 351-358. https://doi.org/10.1016/j.tsf.2016.08.062.

[8] Y.-J. Chen, L.-Y. Chen, Effect of Morphology Control on Hematite Nanostructures for Solar Water Splitting, Energy Procedia, 61 (2014) 2046-2049. https://doi.org/10.1016/j.egypro.2014.12.072.

[9] P. Liao, M.C. Toroker, E.A. Carter, Electron transport in pure and doped hematite, Nano Lett., 11 (2011) 1775-1781. https://doi.org/10.1021/nl200356n.

[10] Z. Li, W. Luo, M. Zhang, J. Feng, Z. Zou, Photoelectrochemical cells for solar hydrogen production: current state of promising photoelectrodes, methods to improve their properties, and outlook, Energy Environ. Sci., 6 (2013) 347-370. https://doi.org/10.1039/C2EE22618A.

[11] I. Cesar, K. Sivula, A. Kay, R. Zboril, M. Grätzel, Influence of feature size, film thickness, and silicon doping on the performance of nanostructured hematite photoanodes for solar water splitting, J. Phys. Chem. C, 113 (2009) 772-782. https://doi.org/10.1021/jp809060p.

[12] Y. Hu, D.K. Bora, F. Boudoire, F. Häussler, M. Graetzel, E.C. Constable, A. Braun, A dip coating process for large area silicon-doped high performance hematite photoanodes, J. Renew. Sustain. Energy, 5 (2013). https://doi.org/10.1063/1.4812831.

[13] F.L. Souza, K.P. Lopes, P.A. Nascente, E.R. Leite, Nanostructured hematite thin films produced by spin-coating deposition solution: Application in water splitting, Sol. Energy Mater. Sol. Cells, 93 (2009) 362-368. https://doi.org/10.1016/j.solmat.2008.11.049.

[14] J. Talibawo, P.I. Kyesmen, M.C. Cyulinyana, M. Diale, Facile Zn and Ni Co-doped hematite nanorods for efficient photocatalytic water oxidation, Nanomaterials, 12 (2022) 2961. https://doi.org/10.3390/nano12172961.

[15] K.H. Abass, Fe2O3 thin films prepared by spray pyrolysis technique and study the annealing on its optical properties, Int. Lett. Chem., Phys. Astron., 6 (2015) 24-31. https://doi.org/10.56431/p-579km4.

[16] Z. Landolsi, I.B. Assaker, R. Chtourou, S. Ammar, Photoelectrochemical impedance spectroscopy of electrodeposited hematite α-Fe 2 O 3 thin films: effect of cycle numbers, J. Mater. Sci.: Mater. Electron., 29 (2018) 8176-8187. https://doi.org/10.1007/s10854-018-8824-7.

[17] Q. Wu, K. Zhang, D. Wang, Y. Lin, T. Xie, Dual-suppression of bulk and surface charges recombination for hematite photoanode, Electrochim. Acta, 449 (2023) 142241. https://doi.org/10.1016/j.electacta.2023.142241.

[18] Q. Zeng, J. Bai, J. Li, L. Xia, K. Huang, X. Li, B. Zhou, A novel in situ preparation method for nanostructured α-Fe 2 O 3 films from electrodeposited Fe films for efficient photoelectrocatalytic water splitting and the degradation of organic pollutants, J. Mater. Chem. A, 3 (2015) 4345-4353. https://doi.org/10.1039/C4TA06017B.

[19] S. Tang, J. Zhang, S. Wu, C. Hu, Y. Li, L. Jiang, Q. Cui, Effects of heating rate on the nucleation, growth, and transformation of InOOH and In2O3 via solvothermal reactions, J. Phys. Chem. C, 118 (2014) 21170-21176. https://doi.org/10.1021/jp505459z.

[20] A. Kleiman-Shwarsctein, Y.-S. Hu, A.J. Forman, G.D. Stucky, E.W. McFarland, Electrodeposition of α-Fe2O3 doped with Mo or Cr as photoanodes for photocatalytic water splitting, J. Phys. Chem. C, 112 (2008) 15900-15907. https://doi.org/10.1021/jp803775j.

[21] P.I. Kyesmen, N. Nombona, M. Diale, Effects of Film Thickness and Coating Techniques on the Photoelectrochemical Behaviour of Hematite Thin Films, Front. Energy Res., 9 (2021) 683293. https://doi.org/10.3389/fenrg.2021.683293.

[22] N. Zhao, Y. Sui, M. Ma, T. Wang, C. Miao, Z. Wang, L. Yang, F. Wang, B. Yao, Optimized grain growth for efficient solution-processed Bi-doped Cu2ZnSn (S, Se) 4 thin film solar cells via spin-coated layers adjustment and two-step selenization, Ceram. Int., (2024). https://doi.org/10.1016/j.ceramint.2024.01.010.

[23] E.R. Shaaban, N. Afify, A. El-Taher, Effect of film thickness on microstructure parameters and optical constants of CdTe thin films, J. Alloys Compd., 482 (2009) 400-404. https://doi.org/10.1016/j.jallcom.2009.04.033.

[24] R. Nithiyavathi, S.J. Sundaram, G.T. Anand, D.R. Kumar, A.D. Raj, D.A. Al Farraj, R.M. Aljowaie, M.R. AbdelGawwad, Y. Samson, K. Kaviyarasu, Gum mediated synthesis and

characterization of CuO nanoparticles towards infectious disease-causing antimicrobial resistance microbial pathogens, J. Infect. Public Health, 14 (2021) 1893-1902. https://doi.org/10.1016/j.jiph.2021.10.022.

[25] D.R. Uhlmann, Nucleation, crystallization and glass formation, J. Non-Cryst. Solids, 38 (1980) 693-698. https://doi.org/10.1016/0022-3093(80)90517-7.

[26] P.M. Martin, Handbook of deposition technologies for films and coatings: science, applications and technology, William Andrew, 2009.

[27] G.-L. Yang, X. Lin, M.-H. Song, Q. Hu, Z.-T. Wang, W.-D. Huang, Decline of nucleation in the heating process with a high heating rate, Chin. Phys. B, 23 (2014) 086401. https://doi.org/10.1088/1674-1056/23/8/086401.

[28] P.I. Kyesmen, N. Nombona, M. Diale, Modified annealing approach for preparing multi-layered hematite thin films for photoelectrochemical water splitting, Mater. Res. Bull., 131 (2020) 110964. https://doi.org/10.1016/j.materresbull.2020.110964.

[29] H. Kim, J. Horwitz, G. Kushto, A. Pique, Z. Kafafi, C. Gilmore, D. Chrisey, Effect of film thickness on the properties of indium tin oxide thin films, J. Appl. Phys., 88 (2000) 6021-6025. https://doi.org/10.1063/1.1318368.

[30] A.A. Akl, I. El Radaf, A.S. Hassanien, An extensive comparative study for microstructural properties and crystal imperfections of Novel sprayed Cu3SbSe3 Nanoparticle-thin films of different thicknesses, Optik, 227 (2021) 165837. https://doi.org/10.1016/j.ijleo.2020.165837.

[31] C. Xu, B.C.S. Varaprasad, D.E. Laughlin, J.-G. Zhu, Bias sputtering of granular L10-FePt films with hexagonal boron nitride grain boundaries, Sci. Rep., 13 (2023) 11087. https://doi.org/10.1038/s41598-023-38106-9.

[32] Z. Braiek, M. Gannouni, I.B. Assaker, A. Bardaoui, A. Lamouchi, A. Brayek, R. Chtourou, Correlation between physical properties and growth mechanism of In2S3 thin films fabricated by electrodeposition technique with different deposition times, Eur. Phys. J-Appl. Phys., 72 (2015) 10302. https://doi.org/10.1051/epjap/2015150195.

[33] N. Revathi, P. Prathap, K.R. Reddy, Thickness dependent physical properties of close space evaporated In2S3 films, Solid State Sci., 11 (2009) 1288-1296. https://doi.org/10.1016/j.solidstatesciences.2009.04.019

[34] G. Liu, Y. Li, Y. Xiao, D. Jia, C. Li, J. Zheng, X. Liu, Nanoporous Fe-doped BiVO 4 Modified with MIL-53 (Fe) for Enhanced Photoelectrochemical Stability and Water Splitting Perfromances, Catal. Lett., 149 (2019) 870-875. https://doi.org/10.1007/s10562-018-2629-4.

[35] F. Chen, T. Ma, T. Zhang, Y. Zhang, H. Huang, Atomic-level charge separation strategies in semiconductor-based photocatalysts, Adv. Mater., 33 (2021) 2005256. https://doi.org/10.1002/adma.202005256.

[36] F. Pellegrino, L. Pellutiè, F. Sordello, C. Minero, E. Ortel, V.-D. Hodoroaba, V. Maurino, Influence of agglomeration and aggregation on the photocatalytic activity of TiO2 nanoparticles, Appl. Catal. B, 216 (2017) 80-87. https://doi.org/10.1016/j.apcatb.2017.05.046.

[37] A. Bak, W. Choi, H. Park, Enhancing the photoelectrochemical performance of hematite (α-Fe2O3) electrodes by cadmium incorporation, Appl. Catal. B, 110 (2011) 207-215. https://doi.org/10.1016/j.apcatb.2011.09.002.

[38] K. Sivula, F. Le Formal, M. Grätzel, Solar water splitting: progress using hematite (α-Fe2O3) photoelectrodes, ChemSusChem, 4 (2011) 432-449. https://doi.org/10.1002/cssc.201000416.

[39] H.-J. Ahn, M.-J. Kwak, J.-S. Lee, K.-Y. Yoon, J.-H. Jang, Nanoporous hematite structures to overcome short diffusion lengths in water splitting, J. Mater. Chem. A, 2 (2014) 19999-20003. https://doi.org/10.1039/C4TA04890C.

[40] S.Y. Chae, G. Rahman, O.-s. Joo, Elucidation of the structural and charge separation properties of titanium-doped hematite films deposited by electrospray method for photoelectrochemical water oxidation, Electrochim. Acta, 297 (2019) 784-793. https://doi.org/10.1016/j.electacta.2018.11.166.

[41] W. Mäntele, E. Deniz, UV–VIS absorption spectroscopy: Lambert-Beer reloaded, in, Elsevier, 2017, pp. 965-968. https://doi.org/10.1016/j.saa.2016.09.037.

[42] B. Chen, H. Wu, S.F.Y. Li, Development of variable pathlength UV–vis spectroscopy combined with partial-least-squares regression for wastewater chemical oxygen demand (COD) monitoring, Talanta, 120 (2014) 325-330. https://doi.org/10.1016/j.talanta.2013.12.026.

[43] J.S. Nyarige, T.P. Krüger, M. Diale, Structural and optical properties of hematite and L-arginine/hematite nanostructures prepared by thermal spray pyrolysis, Surf. Interfaces, 18 (2020) 100394. https://doi.org/10.1016/j.surfin.2019.100394.

[44] E. Nurlaela, A. Ziani, K. Takanabe, Tantalum nitride for photocatalytic water splitting: concept and applications, Mater. Renew. Sustain. Energy, 5 (2016) 1-21. https://doi.org/10.1007/s40243-016-0083-z.

[45] D.K. Bora, The photocathodic behavior of hierarchical ZnO/hematite hetero nanoarchitectures, J. Mater. Res., 31 (2016) 1554-1564. https://doi.org/10.1557/jmr.2016.107.

[46] M. Baikov, A. Ponyavina, A. Prishivalko, V. Sviridov, N. Sil'Vanovich, Effect of the microstructure of closely packed ultradisperse hematite layers on their spectral properties, J. Appl. Spectrosc., 63 (1996) 297-303. https://doi.org/10.1007/BF02606589.

[47] P.I. Kyesmen, N. Nombona, M. Diale, Influence of coating techniques on the optical and structural properties of hematite thin films, Surf. Interfaces, 17 (2019) 100384. https://doi.org/10.1016/j.surfin.2019.100384.

[48] Y.-H. Chen, K.-J. Tu, Thickness dependent on photocatalytic activity of hematite thin films, Int. J. Photoenergy, 2012 (2012). https://doi.org/10.1155/2012/980595.

[49] S. Senthilarasu, R. Sathyamoorthy, S. Lalitha, A. Subbarayan, K. Natarajan, Thermally evaporated ZnPc thin films—band gap dependence on thickness, Sol. Energy Mater. Sol. Cells, 82 (2004) 179-186. https://doi.org/10.1016/j.solmat.2004.01.016.

[50] Y.L. Huang, Y. Chen, W. Zhang, S.Y. Quek, C.-H. Chen, L.-J. Li, W.-T. Hsu, W.-H. Chang, Y.J. Zheng, W. Chen, Bandgap tunability at single-layer molybdenum disulphide grain boundaries, Nat. Commun., 6 (2015) 6298. https://doi.org/10.1038/ncomms7298.

[51] M. Öztas, M. Bedir, Thickness dependence of structural, electrical and optical properties of sprayed ZnO: Cu films, Thin Solid Films, 516 (2008) 1703-1709. https://doi.org/10.1016/j.tsf.2007.05.018.

[52] B. Iandolo, H. Zhang, B. Wickman, I. Zorić, G. Conibeer, A. Hellman, Correlating flat band and onset potentials for solar water splitting on model hematite photoanodes, RSC Adv., 5 (2015) 61021-61030. https://doi.org/10.1039/C5RA10215D.

[53] M. Vanags, A. Šutka, J. Kleperis, P. Shipkovs, Comparison of the electrochemical properties of hematite thin films prepared by spray pyrolysis and electrodeposition, Ceram. Int., 41 (2015) 9024-9029. https://doi.org/10.1016/j.ceramint.2015.03.272.

[54] V. Aroutiounian, V. Arakelyan, G. Shahnazaryan, H. Hovhannisyan, H. Wang, J.A. Turner, Photoelectrochemistry of tin-doped iron oxide electrodes, Sol. Energy, 81 (2007) 1369-1376. https://doi.org/10.1016/j.solener.2007.01.006.

[55] F. La Mantia, H. Habazaki, M. Santamaria, F. Di Quarto, A critical assessment of the Mott-Schottky analysis for the characterisation of passive film-electrolyte junctions, Russ. J. Electrochem., 46 (2010) 1306-1322. https://doi.org/10.1134/S102319351011011X.

[56] H. Li, D. Niu, D. Liu, W. Huang, X. Zhang, Understanding the enhanced photoelectrochemical activity of Ta doped hematite, J. Mol. Struct., 1139 (2017) 104-110. https://doi.org/10.1016/j.molstruc.2017.03.008.

[57] X. Cheng, X. Li, L. Yang, C. Du, Corrosion resistance of 316L stainless steel in acetic acid by EIS and Mott-Schottky, J. Wuhan Univ. Technol., Mater. Sci. Ed., 23 (2008) 574-578. https://doi.org/10.1007/s11595-006-4574-0.

[58] T. Wijesinghe, D.J. Blackwood, Electrochemical and photoelectrochemical characterization of the passive film formed on AISI 254SMO super-austenitic stainless steel, J. Electrochem. Soc., 154 (2006) C16. https://doi.org/10.1149/1.2382269.

[59] H. Chen, Z. Wei, K. Yan, Y. Bai, Z. Zhu, T. Zhang, S. Yang, Epitaxial growth of ZnO nanodisks with large exposed polar facets on nanowire arrays for promoting photoelectrochemical water splitting, Small, 10 (2014) 4760-4769. https://doi.org/10.1002/smll.201401298.

[60] A.A. Tahir, K.U. Wijayantha, Photoelectrochemical water splitting at nanostructured ZnFe2O4 electrodes, J. Photochem. Photobiol. A: Chem., 216 (2010) 119-125. https://doi.org/10.1016/j.jphotochem.2010.07.032.

[61] L. Xi, K.M. Lange, Surface modification of hematite photoanodes for improvement of photoelectrochemical performance, Catalysts, 8 (2018) 497. https://doi.org/10.3390/catal8110497.

[62] F. Wu, Y. Chang, W. Zhai, J. Wang, Ultrasonic passivated hematite photoanode with efficient hole transfer pathway for enhanced photoelectrochemical water oxidation, J. Mater. Sci., 57 (2022) 14936-14947. https://doi.org/10.1007/s10853-022-07458-4.

[63] T. Lopes, L. Andrade, F. Le Formal, M. Gratzel, K. Sivula, A. Mendes, Hematite photoelectrodes for water splitting: evaluation of the role of film thickness by impedance spectroscopy, PCCP, 16 (2014) 16515-16523. https://doi.org/10.1039/C3CP55473B.

[64] B. Eftekharinia, A. Moshaii, A. Dabirian, N.S. Vayghan, Optimization of charge transport in a Co–Pi modified hematite thin film produced by scalable electron beam evaporation for photoelectrochemical water oxidation, J. Mater. Chem. A, 5 (2017) 3412-3424. https://doi.org/10.1039/C6TA09331K.

[65] A.Y. Ahmed, M.G. Ahmed, T.A. Kandiel, Hematite photoanodes with size-controlled nanoparticles for enhanced photoelectrochemical water oxidation, Appl. Catal. B, 236 (2018) 117-124. https://doi.org/10.1016/j.apcatb.2018.04.073.

[66] Y. Gönüllü, K. Kelm, S. Mathur, B. Saruhan, Equivalent circuit models for determination of the relation between the sensing behavior and properties of undoped/cr doped TiO2 NTs, Chemosensors, 2 (2014) 69-84. https://doi.org/10.3390/chemosensors2010069.

[67] B. Hirschorn, M.E. Orazem, B. Tribollet, V. Vivier, I. Frateur, M. Musiani, Determination of effective capacitance and film thickness from constant-phase-element parameters, Electrochim. Acta, 55 (2010) 6218-6227. https://doi.org/10.1016/j.electacta.2009.10.065.

[68] P. Dias, A. Mendes, Hydrogen production from photoelectrochemical water splitting, Encyclopedia of Sustainability Science and Technology; Meyers, RA, Ed.; Springer Science and Business Media LLC: Berlin/Heidelberg, Germany, (2017) 1-52. https://hdl.handle.net/10216/117040.

[69] C. Jiang, S.J. Moniz, A. Wang, T. Zhang, J. Tang, Photoelectrochemical devices for solar water splitting–materials and challenges, Chem. Soc. Rev., 46 (2017) 4645-4660. https://doi.org/10.1039/c6cs00306k.

[70] E. Kusmierek, Semiconductor electrode materials applied in photoelectrocatalytic wastewater treatment—an overview, Catalysts, 10 (2020) 439. https://doi.org/10.3390/catal10040439.

[71] S. Xiao, C. Hu, H. Lin, X. Meng, Y. Bai, T. Zhang, Y. Yang, Y. Qu, K. Yan, J. Xu, Integration of inverse nanocone array based bismuth vanadate photoanodes and bandgap-tunable perovskite solar cells for efficient self-powered solar water splitting, J. Mater. Chem. A, 5 (2017) 19091-19097. https://doi.org/10.1039/C7TA06309A.

[72] W. Hamd, S. Cobo, J. Fize, G. Baldinozzi, W. Schwartz, M. Reymermier, A. Pereira, M. Fontecave, V. Artero, C. Laberty-Robert, Mesoporous α-Fe 2 O 3 thin films synthesized via the

sol–gel process for light-driven water oxidation, PCCP, 14 (2012) 13224-13232. https://doi.org/10.1039/C2CP42535A.

[73] N. Al-Aisaee, M. Alhabradi, X. Yang, M. Alruwaili, S. Rasul, A.A. Tahir, Fabrication of WO3/Fe2O3 heterostructure photoanode by PVD for photoelectrochemical applications, Sol. Energy Mater. Sol. Cells, 263 (2023) 112561. https://doi.org/10.1016/j.solmat.2023.112561.

[74] A. Tofanello, A.L. Freitas, W.M. Carvalho Jr, T. Salminen, T. Niemi, F.L. Souza, Hematite surface modification toward efficient sunlight-driven water splitting activity: the role of gold nanoparticle addition, J. Phys. Chem. C, 124 (2020) 6171-6179. https://doi.org/10.1021/acs.jpcc.9b11966.